MATERIALS SCIENCE

Probing the dynamics of nanoparticle formation from a precursor at atomic resolution

Wenpei Gao[1], Peter Tieu[2], Christopher Addiego[3], Yanling Ma[4], Jianbo Wu[4,5,6]*, Xiaoqing Pan[1,3]*

Control of reduction kinetics and nucleation processes is key in materials synthesis. However, understanding of the reduction dynamics in the initial stages is limited by the difficulty of imaging chemical reactions at the atomic scale; the chemical precursors are prone to reduction by the electron beams needed to achieve atomic resolution. Here, we study the reduction of a solid-state Pt precursor compound in an aberration-corrected transmission electron microscope by combining low-dose and in situ imaging. The beam-sensitive Pt precursor, K_2PtCl_4, is imaged at atomic resolution, enabling determination of individual (K, Pt, Cl) atoms. The transformation to Pt nanoclusters is captured in real time, showing a three-stage reaction including the breaking of the ionic bond, formation of $PtCl_2$, and the reduction of the dual-valent Pt to Pt metal. Deciphering the atomic-scale transformation of chemicals in real time using combined low-dose and in situ imaging brings new possibility to study reaction kinetics in general.

INTRODUCTION

Controlling the shape and size of nanoparticles remains a main goal in colloid chemistry to achieve desired electronic, optic, and catalytic properties (*1*–*7*). Especially in catalysis, improved catalytic activity, selectivity, and stability largely depend on the number and types of active sites offered by the surface geometry of nanocatalysts whose growth trajectory must be engineered (*4, 6, 8*). Nanocluster nucleation is one of the key processes during growth. Manipulation of the nucleation kinetics has led to successful synthesis of a group of shaped nanoparticles including nanorods (*9*), nanocubes (*10*), octahedra (*11*), octopod-shaped nanoparticles (*12, 13*), icosahedra (*5*), and other multiply twinned nanoparticles, featuring various enclosing surface features. In general, nucleation is also the initial step in materials synthesis. Without understanding how atoms interact with each other, further improvement on controlling the nucleation kinetics is challenging (*14*). For example, shaped Pt nanoparticles are usually synthesized in a liquid-phase reaction, where chemical compounds consisting of noble metal and ligands such as C–H or Cl^- serve as the precursor; in such a system, current knowledge of Pt cluster nucleation is based on experimental observations that, during growth, the precursor will be reduced by the reducing agent, and the newly formed metal monomers will form small face centered cubic (FCC)/body centered cubic (BCC) clusters owing to the metal-metal interaction. This process is similar to precipitation of solid from the solution. This hypothesis only addresses the kinetics of the reduction process as a whole (*15*–*17*), while direct imaging of the nucleation process covering different stages of the reduction and cluster formation is still missing. A microscopic mechanism detailing the intermediate reaction steps is not available.

Growing nanostructures in the solid phase represents an alternative to materials synthesis in liquid phase. The solid inorganic precursors can be crystalline, where the anion and cation are ionically bonded; for example, K^+ and $PtCl_4^{2-}$ are ionically bonded in K_2PtCl_4. Therefore, under an external trigger, the ionic crystal can dissociate, starting from the weaker bond in solid phase. The reduction process in solid phase may also provide mechanistic insights for reactions in liquid phase, although the redox potential changes depending on the aqueous environment. Studying the reduction process in the solid state can thus help improve the general understanding of materials transformation. Fine control of the growth kinetics is also possible in materials synthesis in the solid state. It has been shown that by using H_2 as the surface adsorbate and reducing gas, Pt and PtNi nanowires can be synthesized in the solid state upon annealing at 250°C (*18*). Such kinetic control offered by a gas molecule adsorbate provides a controlled pathway at the gas-solid interface to grow nanostructures free of organic surfactant, which is usually used in wet chemistry, and thus is easy to apply to scalable production. It is therefore of considerable significance to better understand the kinetic mechanism of the materials transformation from precursors to nanostructures at the atomic scale through observing the ionic bonding breaking.

Another direct benefit of studying the nucleation process in the solid phase is that, without the liquid environment, characterization tools with ultrahigh resolution, such as in situ x-ray nanodiffraction and transmission electron microscopy (TEM), can be applied to resolve the evolving structure in both real and reciprocal space (*19, 20*). For example, the grain rotation and lattice deformation of AgBr have been captured and quantified during the photo-induced chemical reaction of AgBr ➔ Ag + Br, using in situ x-ray nanodiffraction (*19*). In TEM, similarly, if the well-defined lattice from the precursor and interatomic spacing can be probed with a high signal-noise ratio, then the reduction kinetics can be tracked even at the atomic scale. However, most precursors are sensitive to electron beams and are known to be reduced by photo illumination during nanostructure synthesis. In previous research, this sensitivity limited the ability to study the dynamics of the transformation from precursor to nanocluster, as it is nearly impossible to catch the initial atomic structure of the precursor.

Here, we report a study on the atomic resolution imaging of a Pt precursor compound and the dynamics of transformation from precursors to nanoclusters. We are able to resolve the atomic structure using the newly developed low-dose imaging capability provided by the complementary metal-oxide semiconductor–based direct electron detector coupled with a double aberration-corrected transmission electron microscope. The dynamics of different stages of decomposition,

[1]Department of Materials Science and Engineering, University of California, Irvine, CA 92697, USA. [2]Department of Chemistry, University of California, Irvine, CA 92697, USA. [3]Department of Physics and Astronomy, University of California, Irvine, CA 92697, USA. [4]State Key Laboratory of Metal Matrix Composites, School of Materials Science and Engineering, Shanghai Jiao Tong University, Shanghai 200240, China. [5]Center of Hydrogen Science, Shanghai Jiao Tong University, Shanghai 200240, China. [6]Materials Genome Initiative Center, Shanghai Jiao Tong University, Shanghai 200240, China.
*Corresponding author. Email: xiaoqing.pan@uci.edu (X.P.); jianbowu@sjtu.edu.cn (J.W.)

reduction, and nucleation are captured, identified, and revealed. The insight gained with the combined spatial and time resolution leads to a better understanding of the transformation kinetics of Pt from precursors to nanoclusters and is a promising way to study atomic-scale reaction dynamics in general.

RESULTS

K_2PtCl_4 is commonly used as the precursor of Pt nanoparticles in a typical synthesis. Its crystal structure is illustrated in Fig. 1A. For TEM experiments, K_2PtCl_4 was first dissolved in deionized water at a concentration of 0.02 M and dispersed onto the carbon film of a TEM grid. Upon drying, the precursor formed crystallites as shown in Fig. 1B. In the bright-field TEM image (Fig. 1B), the crystallite is around 50 nm by 60 nm in size. Because K_2PtCl_4 can be reduced by electron beam under normal imaging conditions, it is challenging to resolve its pristine atomic structure. We thus weakened the electron beam dose to less than 1 e/A^2·s when taking images and performing electron diffraction to limit possible beam-induced reduction of the sample. Using a similar technique, beam-sensitive materials including metal-organic frameworks and halide perovskite structures have been imaged (*21*). In Fig. 1C, the diffraction pattern exhibits a symmetry of D4h1 (P4/mmm) along the (100) zone axis. High-resolution electron microscopy (HREM) was carried out at 300,000× magnification. Sixty-four images from the same area were taken at an exposure time of 0.1 s each, after which the images were aligned using cross-correlation and averaged. Each individual image does not yield interpretable contrast and intensity from the structure (fig.S1); however, after averaging over 64 images, atomic columns were resolved clearly, as shown in Fig. 1D and fig. S1 to S4 and demonstrated in movie S1.

The high-resolution TEM image in Fig. 1D shows periodic latticed squares with an atom in the center (colored yellow in Fig. 1D and fig. S3) and those without bright atomic contrast in the center (colored blue in Fig. 1D and fig. S3). By comparing the atomic resolution images with the available atomic structure of K_2PtCl_4 (*22*), the element of each individual atom can be identified. The atoms in the corners are K, the atoms in the middle of the edges of the squares are Cl, and those in the center of the square colored yellow are Pt, as shown in Fig. 1 (A, D, F, and G) and fig. S3. The simulated HREM image in Fig. 1E using the atomic structure refined from the experiment also fits well with Fig. 1D and fig. S5. It is noteworthy that the variation of intensities from K and Cl in experimental images compared to those from simulated images comes from two parts, including the possible slight structure tilt away from the accurate zone axis and the low electron dose resulting in the random fluctuation of image intensity.

It has been reported that the reduction of dual-valence Pt(II) to its metallic state can be obtained by electron transfer from inorganic and organic reducing agents, via photodecomposition (*23*), radiolysis

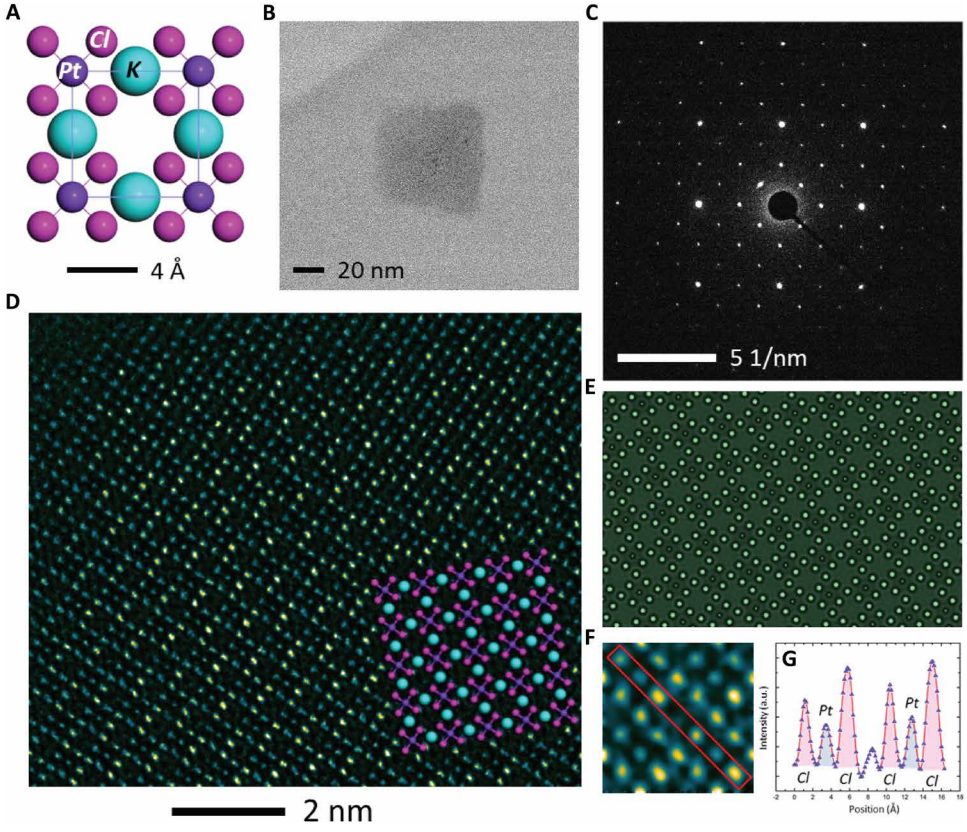

Fig. 1. Low-dose atomic resolution imaging of K_2PtCl_4. (**A**) The atomic model of the K_2PtCl_4 unit cell, with K in cyan, Pt in purple, and Cl in pink. (**B**) Bright-field TEM image of a large K_2PtCl_4 crystallite. (**C**) Diffraction pattern of the K_2PtCl_4 crystallite in (B) after it is tilted along the (001) zone axis. (**D**) Atomic resolution low-dose TEM image of K_2PtCl_4. Dose fractionation was done using an electron dose of 1 e/$Å^2$·s, with 0.1 s for each image. Sixty-four images were acquired, aligned, and averaged. The electron dose then becomes 6.4 e/$Å^2$. The atomic model is overlaid in the inset. (**E**) Simulated HREM image of K_2PtCl_4 with a thickness of 12.3 nm. (**F**) A zoomed-in image of K_2PtCl_4 from a sub-area in (D), and the intensity line profile in arbitrary units (a.u.) from the red box, is shown in (**G**), where the intensity from Pt atoms is located between two Cl atoms.

(*17*), sonochemical reduction (*24*), and a variety of other methods (*25*). In TEM, as imaging electrons are also a reducing agent, either a long exposure time under a low electron dose or elevating the electron beam dose can induce the transformation from a K_2PtCl_4 compound crystallite to Pt nanoclusters. This process is demonstrated in movie S2. Upon increasing the electron beam dose to 30 e/A^2·s, the lattice from K_2PtCl_4, originally visible over the entire area, evolved and eventually developed into separate individual Pt clusters. In Fig. 2, sequential HREM images taken from the video illustrate the formation of a number of Pt nanoclusters. In the zoomed-in images in Fig. 2B, at 1.00 s, the existence of Pt nuclei within the K_2PtCl_4 lattice is initially indicated by the Moiré fringes. The Moiré fringes gradually adopted the FCC lattice of Pt from 1.80 s to 3.80 s, as shown within the areas in the red contours; this is indicative of a Pt cluster inclusion forming within the K_2PtCl_4 lattice matrix. The Pt nanocluster grew more pronounced over time. At 4.00 s, the K_2PtCl_4 lattice broke and then disappeared, leaving the Pt cluster in the center, which indicates that the entire Pt precursor was consumed upon the formation of Pt nanoclusters. Neither lattice from K_2PtCl_4 nor lattice from Pt is observed in the region colored yellow surrounding the Pt cluster (Fig. 2B).

The Pt nanoclusters also form over extended time under low-dose imaging conditions, as shown in fig. S7. A sub-area of the sequential images was selected, and the fast Fourier transformation (FFT) was applied to discern the structure. From the time series FFT patterns in Fig. 3A and fig. S8, the two-dimensional (2D) reciprocal lattice of K_2PtCl_4 can be seen at the beginning and through the entire process until 18:23. This pattern became weak over the course, while other FFT spots appeared and several FFT ring patterns evolved. At 20:51, the FFT ring pattern from Pt is the major feature.

The FFT patterns were then integrated radially. The intensity profile can be compared with powder XRD patterns, as in fig. S9. The beginning FFT intensity profile shows characteristic peaks in the simulated powder XRD from K_2PtCl_4; after 9:55, many reflections disappear. This radially integrated intensity profile from FFT also reflects the radial distribution function (RDF). Peaks in the RDF correspond to atom pairs with certain bond lengths and therefore can be used to identify the species with characteristic periodicity. From the RDF spectra, we see that, from 00:00 to 13:42, the peak at 1.4 1/nm corresponding to the Pt-Pt spacing, the peak at 3.05 1/nm corresponding to the K-K spacing, and the peak at 4.26 1/nm corresponding to the Pt-Cl spacing from K_2PtCl_4 become weaker, while the peak at 3.35 1/nm becomes stronger at 9:55 and remains strong until 16:13. By correlating the reciprocal space with real space, we found that the peak at 3.35 1/nm is from the spacing of Cl-Cl in the form of $[PtCl_4]^{2-}$ and $PtCl_2$. As all other peaks from K_2PtCl_4 fade and disappear, this peak at 3.35 1/nm remains from 9:55 to 16:13, indicating the existence of $[PtCl_4]^{2-}$ in the early stage and $PtCl_2$ later at the intermediate stage. Eventually, the RDF is well fitted with polycrystalline Pt, where the peaks from Pt(111), Pt(200), Pt(220), and Pt(311) planes are more intensive in the end. The Pt(111) peak shifts from 4.74 to 4.65 1/nm in the reciprocal space. Because a larger spacing in reciprocal lattice corresponds to a smaller bond length in real space, the Pt(111) peak shift indicates the change from a smaller lattice spacing to a larger lattice spacing, and therefore, the Pt lattice experiences larger contraction at the beginning of the nucleation and lower contraction when the size of the Pt nanocluster grows. It has been reported that the nanoparticles have a surface contraction of up to 6.3% when their sizes are smaller than 4 nm (*26*). Comparing to the Pt lattice of 3.92 Å [4.42 1/nm for Pt(111)], our in situ results here show a lattice contraction from 6.9 to 5.1% during the growth of Pt nanoclusters. When the nanoclusters grow larger in size, electron scattering by higher index planes becomes stronger; thus, higher-order diffraction from Pt(200), Pt(220), and Pt(311) is seen at 20:51.

We further studied the other ending product in addition to the Pt nanoparticles to trace where the extra species of K and Cl were located. From the high-angle annular dark-field (HAADF) scanning transmission electron microscopy (STEM) image and 2D energy-dispersive spectra (EDS) map in Fig. 4, the particles with brighter

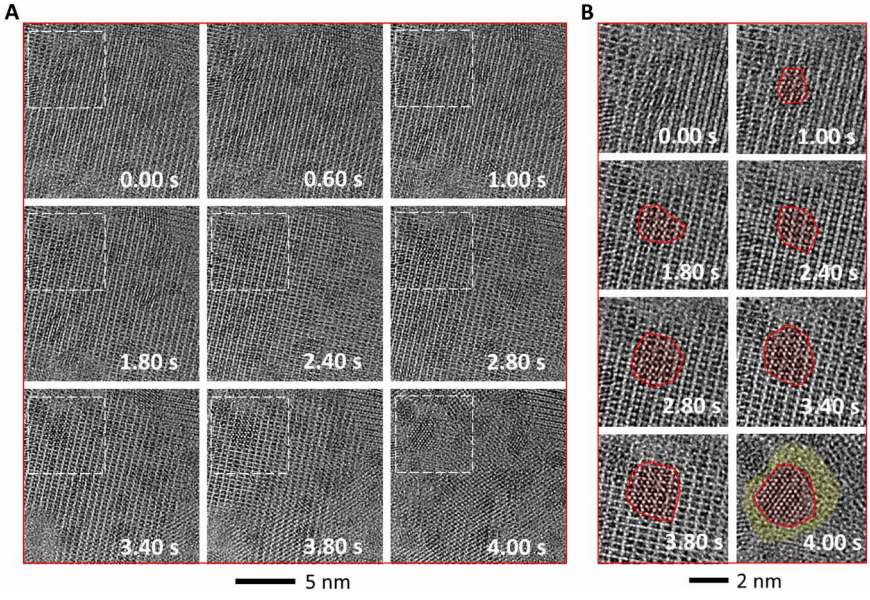

Fig. 2. Evolution of K_2PtCl_4 into Pt nanoparticles. (**A**) Sequential TEM images show the evolution of K_2PtCl_4 into Pt nanoparticles. A Pt nanoparticle nucleation process is shown in the zoomed-in images in (**B**), from the marked sub-area within the white dashed boxes in (A). The red contour lines indicate the edge of the newly formed Pt clusters. The region in yellow highlights the void area without lattice after the formation of a Pt cluster.

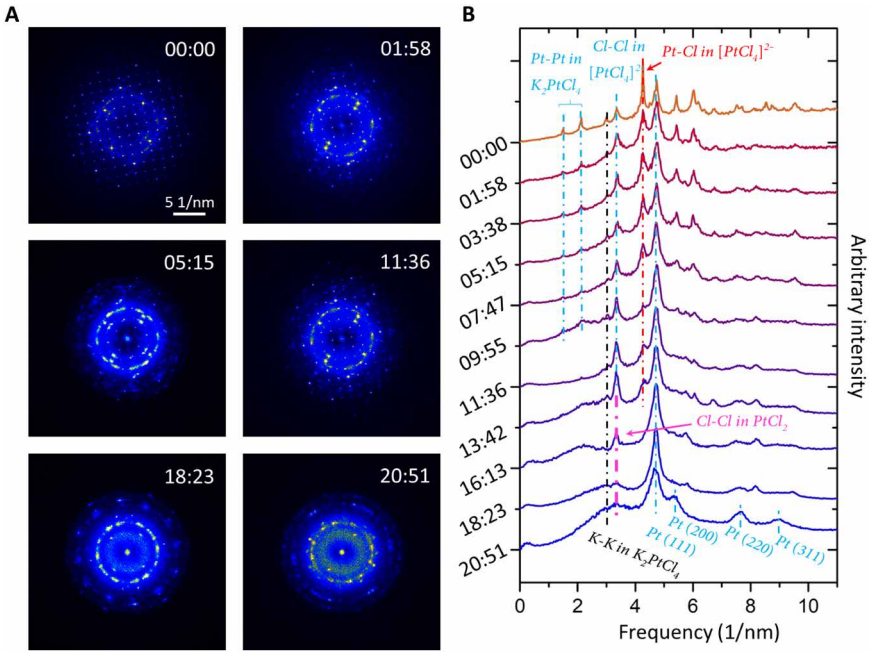

Fig. 3. Sequential RDF during the transformation. (**A**) Time series diffractogram using FFT from sequential low-dose images. (**B**) RDF derived from the sequential diffractogram.

intensity are Pt. In the background, there are signals from K and Cl that are more evenly distributed over the area. The electron energy loss spectroscopy (EELS) in Fig. 4 also shows the K $L_{2,3}$ edge and Cl $L_{2,3}$ edge, indicating the existence of K and Cl from KCl after the formation of Pt nanoparticles.

DISCUSSION

By combining the information from the reaction dynamics captured in real space, the RDF, and the spectroscopy, we propose that the precursor, K_2PtCl_4, first decomposes into K^+ and $PtCl_4^{2-}$ owing to the weaker ionic bonding. $PtCl_4^{2-}$ then decomposes into $PtCl_2$ and Cl^-. This second stage has not been reported in experimental studies, which is now revealed from the FFT of the high-resolution image taken under a low electron dose and high acquisition efficiency. Upon the removal of the K species from the precursor, the lattice became less stable. Compounds including $PtCl_2$, KCl, and Cl_2 can move freely. Eventually, $PtCl_2$ is reduced into Pt, and the formation of the Pt nanoparticle leaves KCl and Cl_2 as the residual species, with Cl_2 in the gas phase and being removed from the TEM column. The zerovalent Pt species either form small nuclei or migrate and grow into larger Pt nanoparticles. This entire process is demonstrated in the atomic models in Fig. 5. Our finding on the staged reduction and nucleation of Pt agrees with that of the free energy in chemical reaction: From the previous calculation (*27*), the transformation of $PtCl_4^{2-} \rightarrow PtCl_2 + 2Cl^-$ has $\Delta G = 28.9$ kcal/mol, and then for $PtCl_2 \rightarrow Pt + Cl_2$, $\Delta G = 18.7$ kcal/mol. Therefore, from the initial precursor to $PtCl_2$, the energy required is 28.9 kcal/mol, and an extra energy of 18.7 kcal/mol is required to further reduce $PtCl_2$ to Pt.

It has been reported that, during the synthesis of Au nanostructures in liquid phase using $AuCl_4^-$ as the precursor, the $AuCl_4^-$ is first reduced to $AuCl_3^-$ with Au–Au bonded to each other and forming a dimer structure; after $AuCl_3^-$ is reduced into $AuCl_2^{2-}$, the $AuCl_2^{2-}$ forms trimer structures (*28*). A similar process of Pt has been predicted in molecular dynamics simulations (*29*), where Pt dimers could be stabilized by Cl^- preferably, and zerovalent Pt clusters are not nucleated directly from the precursor. Experimental results have shown that with a weak/moderate reducing agent, the monovalent Pt dimer could be the first reaction intermediate (*16*), while under strong reduction conditions, Pt species are directly reduced into metallic Pt atoms, which nucleate into Pt nanoparticles. While neither scenario has been observed before, our in situ experiment showed the staged decomposition, reduction, and nucleation process of K_2PtCl_4 into Pt nanoparticles in the solid state. Similar to $AuCl_4^-$, we found that, before the complete reduction of Pt^{2+}, a $PtCl_2$ complex can form. The reduction effect from an electron beam under regular low-dose imaging conditions (30 $e/A^2 \cdot s$) is also comparable to the moderate reducing agent since the precursor was not directly reduced into Pt atoms. In ultralow-dose imaging, the structure of K_2PtCl_4 remains intact through the extended imaging time, demonstrating that the reducing effect from the electron beam with an acceleration energy of 300 keV is negligible within the observation time, when the dose rate is below 1 $e/A^2 \cdot s$.

During the growth of the Pt nanoparticle, multiple processes can take place: The Pt species in the form of $PtCl_4^{2-}$ and $PtCl_2$ nearby can be reduced into single monomers first and deposited onto the Pt cluster; the monomers can also have nonzero valence states, such as Pt^+ or Pt^{2+}; on the other hand, Pt single atoms from small clusters can migrate to the larger ones as well via Ostwald ripening (*30*). Previous studies have shown that for the growth of Ag nanoparticles, successive coalescence and reduction steps can be involved (*31*). Specifically, ion monomers can migrate and attach to a growing cluster before the ion is reduced. They are reduced after the formation of a cluster (*31*). For Pt nanoparticle growth in liquid, studies show that the dynamic process involves a chain reaction, where the reduction of metal complexes can be catalyzed by the metal clusters formed previously (*16, 17*). Here, from our observation showing the Pt nanoparticle growth in a solid-state reaction, the void area, colored yellow,

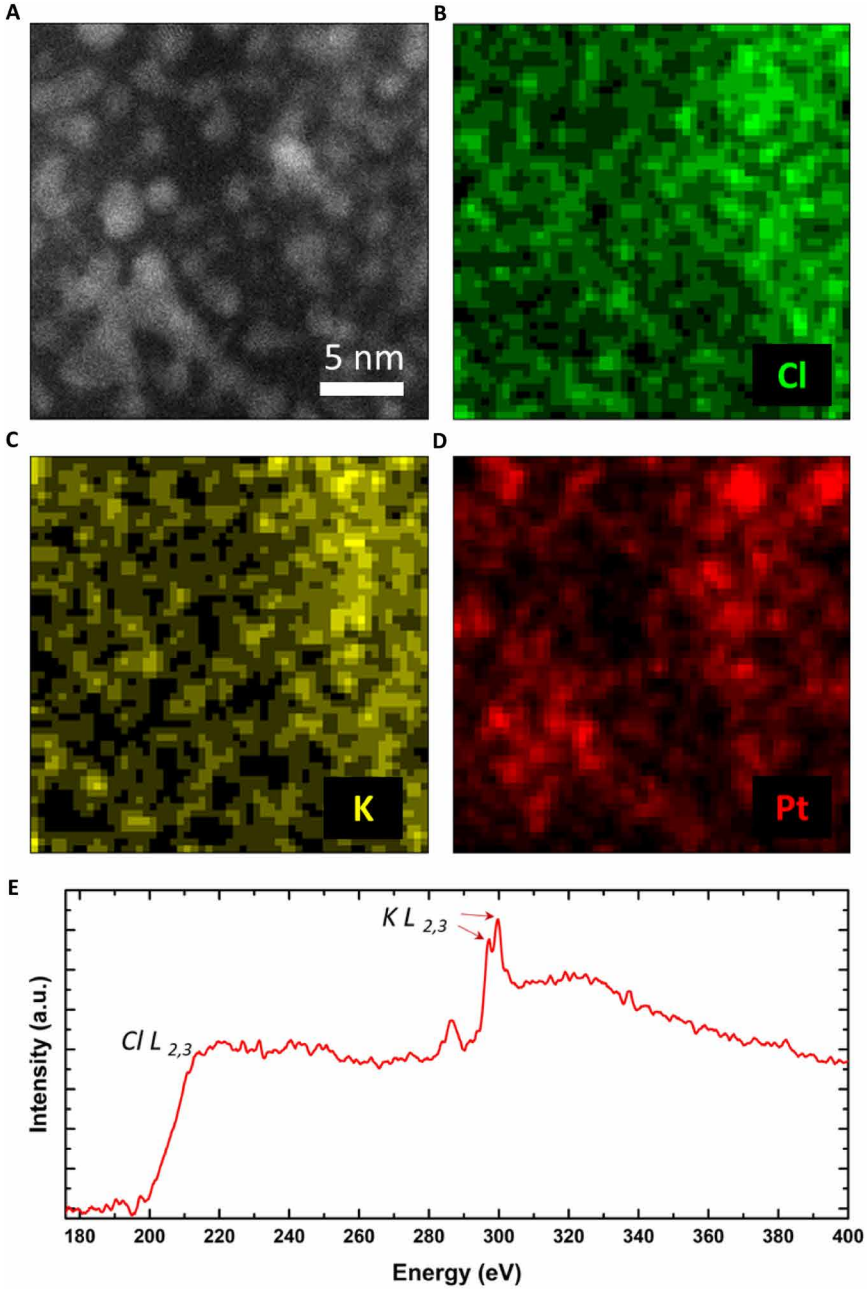

Fig. 4. Composition analysis of the ending product. (**A** to **D**) HAADF image and EDS maps of the ending product of the in situ experiment and (**E**) EELS of the ending product of the in situ experiment showing the existence of Cl and K.

without lattice from either Pt or K_2PtCl_4 in Fig. 2B close to the Pt particles, indicates that either the precursor or Pt zero valence monomers move to Pt nanoparticles. In the former case, Pt nanoparticles grow via self-catalyzing the precursor into a Pt zero-valent state and coalescence.

In general, studying the chemical reaction process in TEM requires the capture of the event at the atomic scale. In liquid, previous in situ studies on the growth of metal nanoparticles have shown that the development of the shape and morphology of nanoparticles can be tracked using liquid cells in TEM (*32*–*34*); however, the trackable particles have larger sizes. For example, Zheng *et al.* (*32, 33*) studied the growth of nanoparticles from 1 nm to 6 to 7 nm. As the observed nanoparticle growth usually started from a size larger than ~1 nm, in projection, this dimension corresponds to the length of three to five atoms. By estimation, for Pt nanoparticles, the size of 1 nm in a Wulff construction corresponds to more than 20 to 25 atoms, which is already well beyond the scale of a nucleation event right after reduction. In the solid state, however, by combining the low-dose high-resolution TEM imaging with in situ observation methods, the acquired image allows for the characterization of both initial atomic structure and intermediate species. The dynamic process can also be analyzed in Fourier space to reveal the kinetics from the evolving RDF related to the bond length between atoms, which provides critical insights into the reduction mechanisms.

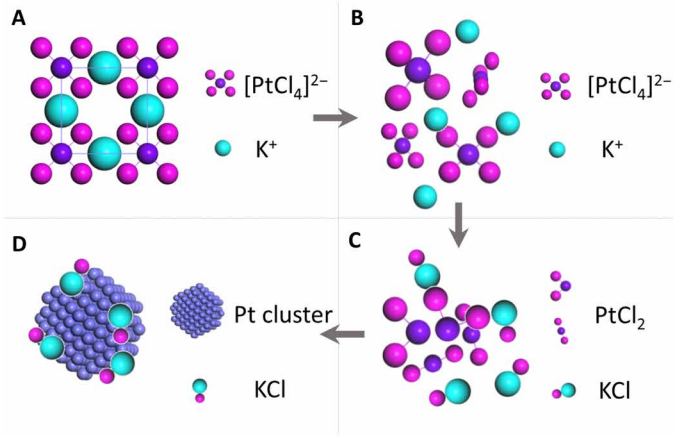

Fig. 5. A schematic showing the evolution of K_2PtCl_4 into Pt nanoparticles. (**A**) K_2PtCl_4, (**B**) dissociation of K^+ and $[PtCl_4]^{2-}$, (**C**) further dissociation into $PtCl_2$ and KCl, and (**D**) nucleation of Pt nanoparticles.

In conclusion, using a new method with combined low-dose and fast imaging, we studied the materials transformation from the precursor of K_2PtCl_4 to Pt nanoparticles in the solid state. The pristine atomic structure of K_2PtCl_4 was revealed at sub-angstrom resolution, with all K, Pt, and Cl atoms resolved. In the in situ experiment, the captured dynamics show that the reduction is via multiple stages: the decomposition to K^+ and $[PtCl_4]^{2-}$, the transformation from $[PtCl_4]^{2-}$ to $PtCl_2$, and the reduction of dual-valent Pt^{2+} to Pt. These processes take place following the order of chemical and bonding energy and simultaneously. The newly formed Pt nanoparticles may also serve as a catalyst in the reduction of the precursor. Such a study not only reveals the dynamic process at the atomic scale but also can explain the general kinetics taking place in the chemical reaction. This method could also be applied to study materials transformation in general. For example, in gas cells, by introducing H_2 as the surface adsorbate and reducing gas, we observed the formation of Pt nanowires in the solid state using in situ TEM (*18*); the existence of H_2 can also lead to the shape change of spherical PdCu nanocrystals to cubes (*35*). When combined with low-dose imaging, in situ imaging could provide more insight into how to further modify the reaction path in the solid state to make size- and shape-specific structures and could benefit the applications of nanostructures on new energy, environmental remedy, nanomedicine, etc.

MATERIALS AND METHODS

Sample preparation

Potassium tetrachloroplatinate (K_2PtCl_4, 98%) was purchased from Aladdin. K_2PtCl_4 (41.51 mg) was dispersed into 5 ml of deionized water and sonicated for 10 min. Two microliters of this aqueous precursor solution was then dispersed onto an amorphous carbon TEM grid (SPI Supplies) and dried in air before low-dose and in situ imaging.

Electron microscopy

HREM was carried out using JEOL-JEM300CF double aberration-corrected TEM at Irvine Materials Research Institute. The TEM was operated at 300 kV with both an image aberration corrector and a probe corrector. Before the HREM imaging, the small crystal of K_2PtCl_4 was tilted along the (001) zone axis according to the diffraction pattern. For low-dose imaging of the Pt precursor, a Gatan K2 camera was used in dose-fractionation mode, where an image with a long exposure time can be taken sequentially with multiple frames each acquired at segmented exposure times. The image size is 4k by 4k pixels. Electron dose was controlled at 1 e/Å^2·s. The transformation of K_2PtCl_4 to Pt nanoclusters was captured using a Gatan OneView camera in in situ mode at a speed of 25 fps with a frame size of 4k by 4k pixels at a dose of 30 e/Å^2·s.

HREM images were simulated using the multislice method in Zmult software package (*36*). The sample thickness was 12 nm. The image parameters used in the simulation were adjusted according to the experimental condition on JEOL JEM-300CF (300 keV, $C_c = 10\,\mu m$, $C_s = 1\,\mu m$).

To identify the composition of the ending product and their distribution, HAADF STEM imaging, EDS, and EELS were carried out on the sample after the in situ experiment and also on JEOL JEM300CF STEM. EDS was acquired using the dual high-speed high–solid angle SDD detectors. EELS was acquired using the GATAN GIF Quantum 965 system. The EELS spectra were taken in both the sample areas and adjacent carbon support. In Fig. 4, the reference spectrum from carbon was subtracted to show L edges from K and Cl.

SUPPLEMENTARY MATERIALS

Supplementary material for this article is available at http://advances.sciencemag.org/cgi/content/full/5/1/eaau9590/DC1

Fig. S1. Low-dose TEM image of K_2PtCl_4.
Fig. S2. Atomic resolution low-dose TEM image of K_2PtCl_4.
Fig. S3. Zoomed-in image and atomic model of K_2PtCl_4.
Fig. S4. Low-dose TEM image and diffraction pattern of K_2PtCl_4.
Fig. S5. HREM simulation of K_2PtCl_4.
Fig. S6. Small Pt clusters grown on the matrix of K_2PtCl_4.
Fig. S7. Sequential low-dose TEM images of K_2PtCl_4.
Fig. S8. Sequential FFT and RDF.
Fig. S9. Analysis of the time-evolving RDF.
Movie S1. Low-dose HREM of the K_2PtCl_4 crystal using K2 dose fractionation.
Movie S2. In situ imaging of the reduction dynamics and the formation of Pt clusters.

REFERENCES AND NOTES

1. Y. Sun, Y. Xia, Shape-controlled synthesis of gold and silver nanoparticles. *Science* **298**, 2176–2179 (2002).
2. S. E. Habas, H. Lee, V. Radmilovic, G. A. Somorjai, P. Yang, Shaping binary metal nanocrystals through epitaxial seeded growth. *Nat. Mater.* **6**, 692–697 (2007).
3. C. Wang, Y. Hu, C. M. Lieber, S. Sun, Ultrathin Au nanowires and their transport properties. *J. Am. Chem. Soc.* **130**, 8902–8903 (2008).
4. T. S. Ahmadi, Z. L. Wang, T. C. Green, A. Henglein, M. A. El-Sayed, Shape-controlled synthesis of colloidal platinum nanoparticles. *Science* **272**, 1924–1925 (1996).
5. J. Wu, A. Gross, H. Yang, Shape and composition-controlled platinum alloy nanocrystals using carbon monoxide as reducing agent. *Nano Lett.* **11**, 798–802 (2011).
6. W. Zhou, J. Wu, H. Yang, Highly uniform platinum icosahedra made by hot injection-assisted GRAILS method. *Nano Lett.* **13**, 2870–2874 (2013).
7. C. Burda, X. Chen, R. Narayanan, M. A. El-Sayed, Chemistry and properties of nanocrystals of different shapes. *Chem. Rev.* **105**, 1025–1102 (2005).
8. J. Turkevich, G. Kim, Palladium: Preparation and catalytic properties of particles of uniform size. *Science* **169**, 873–879 (1970).
9. A. Gole, C. J. Murphy, Seed-mediated synthesis of gold nanorods: Role of the size and nature of the seed. *Chem. Mater.* **16**, 3633–3640 (2004).
10. Q. Zhang, W. Li, C. Moran, J. Zeng, J. Chen, L.-P. Wen, Y. Xia, Seed-mediated synthesis of Ag nanocubes with controllable edge lengths in the range of 30–200 nm and comparison of their optical properties. *J. Am. Chem. Soc.* **132**, 11372–11378 (2010).
11. J. Wu, J. Zhang, Z. Peng, S. Yang, F. T. Wagner, H. Yang, Truncated octahedral Pt_3Ni oxygen reduction reaction electrocatalysts. *J. Am. Chem. Soc.* **132**, 4984–4985 (2010).
12. H. Zhang, M. Jin, Y. Xia, Noble-metal nanocrystals with concave surfaces: Synthesis and applications. *Angew. Chem. Int. Ed.* **51**, 7656–7673 (2012).
13. M. J. Mulvihill, X. Y. Ling, J. Henzie, P. Yang, Anisotropic etching of silver nanoparticles for plasmonic structures capable of single-particle SERS. *J. Am. Chem. Soc.* **132**, 268–274 (2010).

14. Y. Xia, Y. Xiong, B. Lim, S. E. Skrabalak, Shape-controlled synthesis of metal nanocrystals: Simple chemistry meets complex physics? *Angew. Chem. Int. Ed.* **48**, 60–103 (2009).
15. D. G. Duff, P. P. Edwards, B. F. G. Johnson, Formation of a polymer-protected platinum sol: A new understanding of the parameters controlling morphology. *J. Phys. Chem.* **99**, 15934–15944 (1995).
16. A. Henglein, M. Giersig, Reduction of Pt(II) by H_2: Effects of citrate and NaOH and reaction mechanism. *J. Phys. Chem. B* **104**, 6767–6772 (2000).
17. A. Henglein, B. G. Ershov, M. Malow, Absorption spectrum and some chemical reactions of colloidal platinum in aqueous solution. *J. Phys. Chem.* **99**, 14129–14136 (1995).
18. Y. Ma, W. Gao, H. Shan, W. Chen, W. Shang, P. Tao, C. Song, C. Addiego, T. Deng, X. Pan, J. Wu, Platinum-based nanowires as active catalysts toward oxygen reduction reaction: In situ observation of surface-diffusion-assisted, solid-state oriented attachment. *Adv. Mater.* **29**, 1703460 (2017).
19. Z. Huang, M. Bartels, R. Xu, M. Osterhoff, S. Kalbfleisch, M. Sprung, A. Suzuki, Y. Takahashi, T. N. Blanton, T. Salditt, J. Miao, Grain rotation and lattice deformation during photoinduced chemical reactions revealed by in situ X-ray nanodiffraction. *Nat. Mater.* **14**, 691–695 (2015).
20. F. Panciera, Y.-C. Chou, M. C. Reuter, D. Zakharov, E. A. Stach, S. Hofmann, F. M. Ross, Synthesis of nanostructures in nanowires using sequential catalyst reactions. *Nat. Mater.* **14**, 820–825 (2015).
21. Y. Zhu, J. Ciston, B. Zheng, X. Miao, C. Czarnik, Y. Pan, R. Sougrat, Z. Lai, C.-E. Hsiung, K. Yao, I. Pinnau, M. Pan, Y. Han, Unravelling surface and interfacial structures of a metal–organic framework by transmission electron microscopy. *Nat. Mater.* **16**, 532–536 (2017).
22. R. H. B. Mais, P. G. Owston, A. M. Wood, The crystal structure of K_2PtCl_4 and K_2PdCl_4 with estimates of the factors affecting accuracy. *Acta Crystallogr. Sect. B* **28**, 393 (1972).
23. N. Toshima, K. Nakata, H. Kitoh, Giant platinum clusters with organic ligands: Preparation and catalysis. *Inorg. Chim. Acta* **265**, 149–153 (1997).
24. Y. Mizukoshi, R. Oshima, Y. Maeda, Y. Nagata, Preparation of platinum nanoparticles by sonochemical reduction of the Pt(II) ion. *Langmuir* **15**, 2733–2737 (1999).
25. J. Wu, H. Yang, Platinum-based oxygen reduction electrocatalysts. *Acc. Chem. Res.* **46**, 1848–1857 (2013).
26. W. J. Huang, R. Sun, J. Tao, L. D. Menard, R. G. Nuzzo, J. M. Zuo, Coordination-dependent surface atomic contraction in nanocrystals revealed by coherent diffraction. *Nat. Mater.* **7**, 308–313 (2008).
27. X. Xu, J. Kua, R. A. Periana, W. A. Goddard, Structure, bonding, and stability of a catalytica platinum(II) catalyst: A computational study. *Organometallics* **22**, 2057–2068 (2003).
28. T. Yao, Z. Sun, Y. Li, Z. Pan, H. Wei, Y. Xie, M. Nomura, Y. Niwa, W. Yan, Z. Wu, Y. Jiang, Q. Liu, S. Wei, Insights into initial kinetic nucleation of gold nanocrystals. *J. Am. Chem. Soc.* **132**, 7696–7701 (2010).
29. L. Colombi Ciacchi, W. Pompe, A. De Vita, Initial nucleation of platinum clusters after reduction of K_2PtCl_4 in aqueous solution: A first principles study. *J. Am. Chem. Soc.* **123**, 7371–7380 (2001).
30. S. B. Simonsen, I. Chorkendorff, S. Dahl, M. Skoglundh, J. Sehested, S. Helveg, Ostwald ripening in a Pt/SiO_2 model catalyst studied by in situ TEM. *J. Catal.* **281**, 147–155 (2011).
31. J. M. Belloni, M. Mostafavi, in *Metal Clusters in Chemistry*, P. Braunstein, L. A. Oro, P. R. Raithby, Eds. (Wiley-VHC, 1999), pp. 1213–1247.
32. H.-G. Liao, D. Zherebetskyy, H. Xin, C. Czarnik, P. Ercius, H. Elmlund, M. Pan, L.-W. Wang, H. Zheng, Facet development during platinum nanocube growth. *Science* **345**, 916–919 (2014).
33. H. Zheng, R. K. Smith, Y.-w. Jun, C. Kisielowski, U. Dahmen, A. P. Alivisatos, Observation of single colloidal platinum nanocrystal growth trajectories. *Science* **324**, 1309–1312 (2009).
34. J. Wu, W. Gao, J. Wen, D. J. Miller, P. Lu, J.-M. Zuo, H. Yang, Growth of Au on Pt icosahedral nanoparticles revealed by low-dose in situ TEM. *Nano Lett.* **15**, 2711–2715 (2015).
35. Y. Jiang, H. Li, Z. Wu, W. Ye, H. Zhang, Y. Wang, C. Sun, Z. Zhang, In situ observation of hydrogen-induced surface faceting for palladium–copper nanocrystals at atmospheric pressure. *Angew. Chem. Int. Ed.* **55**, 12427–12430 (2016).
36. J. M. S. Zuo, J. C. H. Spence, *Electron Microdiffraction* (Plenum, 1991).

Acknowledgments

Funding: This work was supported by NSF under grant numbers CBET-1159240 and DMR-1506535. TEM work was conducted using the facilities in the Irvine Materials Research Institute (IMRI) at the University of California-Irvine. J.W. acknowledges the support from the thousand talents program for distinguished young scholars from the Chinese government, the National Key R&D Program of China (no. 2017YFB0406000), the NSF of China (21875137, 51521004, and 51420105009), and a start-up fund from Shanghai Jiao Tong University. **Author contributions:** W.G. and X.P. designed the study; W.G., P.T., and C.A. performed the in situ and ex situ TEM experiments, with assistance from Y.M. and J.W.; W.G. carried out the data analysis; W.G. wrote the paper with help from all authors. **Competing interests:** The authors declare that they have no competing interests. **Data and materials availability:** All data needed to evaluate the conclusions in the paper are present in the paper and/or the Supplementary Materials. Additional data related to this paper may be requested from the authors.

Submitted 2 August 2018
Accepted 11 December 2018
Published 25 January 2019
10.1126/sciadv.aau9590

Citation: W. Gao, P. Tieu, C. Addiego, Y. Ma, J. Wu, X. Pan, Probing the dynamics of nanoparticle formation from a precursor at atomic resolution. *Sci. Adv.* **5**, eaau9590 (2019).

Science Advances

Probing the dynamics of nanoparticle formation from a precursor at atomic resolution

Wenpei Gao, Peter Tieu, Christopher Addiego, Yanling Ma, Jianbo Wu and Xiaoqing Pan

Sci Adv **5** (1), eaau9590.
DOI: 10.1126/sciadv.aau9590